MODE-DECOUPLED MEMS GYROSCOPES WITH SILICON-ON-GLASS TECHNOLOGY

Said Emre Alper
Tayfun Akin
Department of Electrical and Electronics Engineering
Middle East Technical University
TR-06531, Balgat-Ankara
Turkey
said@metu.edu.tr / tayfun-akin@metu.edu.tr

1. Introduction

The progress in micromachined vibratory gyroscopes starting from the beginning of 1990s enabled their use in newborn rate-grade applications, where low-cost and small-size is essential, such as in the widespread automotive market [1, 2]. However, the performance of microgyroscopes continuously increased within the past decade approaching to the performance requirements of a number of military tactical-grade applications [3, 4]. It is expected that most of the tactical-grade applications would be dominated by micromachined inertial sensors by year 2020 [5]. One of the major limitations of the microgyroscopes today is the quadrature coupling that arises due to poor manufacturing tolerances compared to the feature size in micromachining technologies [6]. The amount of quadrature coupling can be as high as 1000deg/sec [7]. Although it is possible to minimize the undesired effects of this coupling by phase-sensitive detection, still such a high disturbing signal easily disturbs the linear operating range, scale-factor linearity, and bias stability [8]. There are various approaches reported for reducing quadrature coupling, including electrostatic tuning [7-9], designing the drive electrode with one degree-of-freedom (DOF) motion [10], and designing the sense electrode with one DOF motion [6]. However, most of these designs do not have symmetric suspensions, and therefore, they require dedicated temperature-compensation circuitry. There are also reported symmetric and decoupled gyroscopes with both the drive and the sense electrodes have one DOF, and only the proof mass has two DOF [11-14], for decoupling the drive and sense modes from each other, while reducing temperature-dependent drifts by using symmetric suspensions. It has been achieved to reduce the quadrature coupling down to 70deg/sec by combining the advantages of the symmetric and decoupled gyroscope structure and a high-quality silicon-on-insulator micromachining process [14]. Still, the sense electrodes in those structures are not completely stationary during drive mode vibrations, due to the stresses induced in the flexures coupling the 1-DOF sense electrodes to the 2-DOF proof mass. This fact increases the mechanical cross-talk between the drive and sense modes, and result in a quadrature signal in the order of several tens of deg/sec. Therefore, there is a need for increasing the immunity of the sense electrodes against drive-mode vibrations in order to further reduce quadrature coupling.

This paper presents a 100µm-thick silicon microgyroscope with an improved decoupling arrangement between the drive and sense electrodes in order to minimize mechanical cross-talk and resulting quadrature coupling between the modes. Together with this decoupling arrangement, the structure allows a drive mode oscillation amplitude up to 10µm and at the same time matching the resonance frequencies of the drive and sense modes for enhanced rate sensitivity while keeping mechanical cross-talk as small as possible. The gyroscope is fabricated by thorough etching of a 100µm-thick silicon substrate anodically bonded to a glass handling substrate, while the heating and SOI footing effects of DRIE are eliminated by using a metal etch-stop layer patterned at the bottom of the thin silicon substrate. The gyroscope has capacitive gaps in the order of 5µm yielding an aspect ratio close to 20, and providing a sense capacitance of about 10pF per differential sense electrodes in a total sensor footprint of 4.6x4.2mm^2. The fabricated gyroscope is hybrid connected to a CMOS capacitive interface ASIC, which is fabricated in a commercial 0.6µm CMOS process. The measured quadrature coupling in the fabricated gyroscope is as small as 60deg/sec at atmospheric

Alper, S.E.; Akin, T. (2007) Mode-Decoupled MEMS Gyroscopes with Silicon-on-Glass Technology. In *Military Capabilities Enabled by Advances in Navigation Sensors* (pp. 13-1 – 13-14). Meeting Proceedings RTO-MP-SET-104, Paper 13. Neuilly-sur-Seine, France: RTO. Available from: http://www.rto.nato.int

pressure, limited by electrical crosstalk due to large actuation voltages. Reducing actuation voltages at vacuum also reduce the overall crosstalk and the gyroscope demonstrates an uncompensated quadrature coupling of only 15deg/sec at 50mTorr vacuum. The measured angular rate sensitivity of the gyroscope is 900μV/(deg/sec) and the measured RMS noise-equivalent-rate is 36(deg/hr)/$Hz^{1/2}$ at vacuum. Gyroscope demonstrates an angle random walk of 0.42deg/√hr and bias instability better than 30deg/hr, estimated from the Allan variance analyses.

2. Mode-Decoupled Gyroscope Structure

Figure 1 shows the three-dimensional model (not to scale) of the mode-decoupled gyroscope structure developed in this research. The central proof mass is driven into continuous oscillations along the drive axis (y-axis) by time-varying electrostatic forces generated between stationary and movable drive electrodes. Then, if the base frame, on which the gyroscope is attached, rotates about the sensitive axis (z-axis) with an angular velocity, then the proof mass experience Coriolis forces along the sense-axis (x-axis). The amplitude of oscillation along the sense axis is proportional to the applied angular velocity, which is determined by measuring the capacitance variation between the stationary and movable sense electrodes.

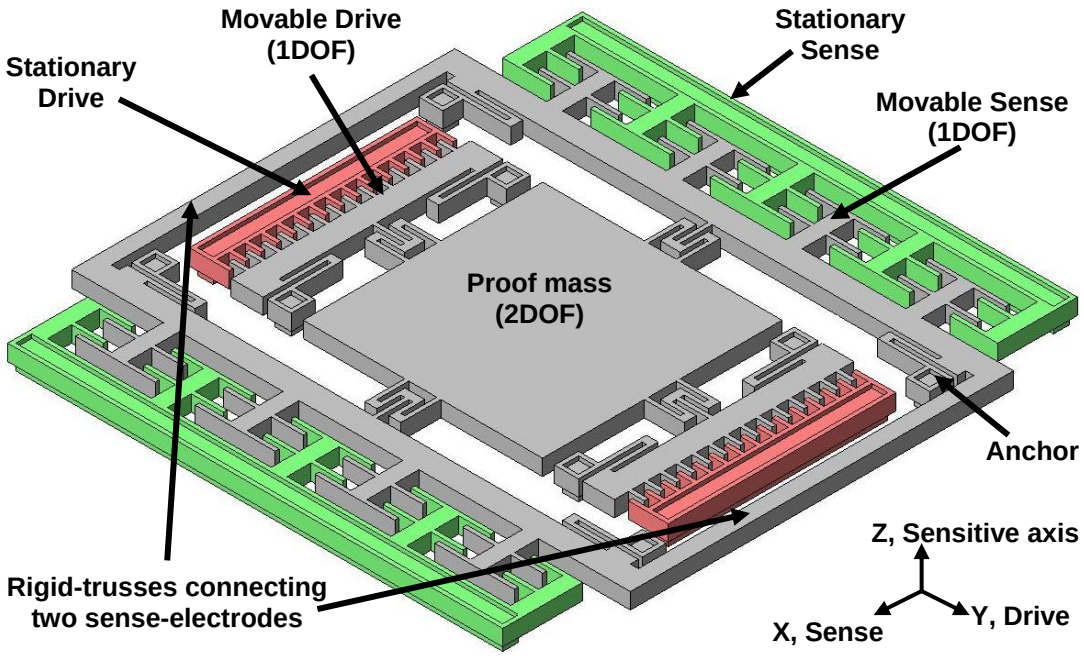

Figure 1: Three-dimensional model (not to scale) of the mode-decoupled gyroscope structure.

The drive mode of the gyroscope is optimized for linear and large amplitude driving oscillations, whereas the sense mode is optimized for increased sensitivity to small capacitive variations and for electrostatic frequency tuning. Suspension flexures are designed symmetric along the drive and sense modes for minimizing possible temperature-dependent drift. Undesired mechanical cross-talk between the drive and sense modes is minimized by proper design of suspension flexures and anchorage of the structure for restricting the motion of the movable drive and sense electrodes to one degree-of-freedom (DOF), while allowing the two DOF motion only for the proof mass. In addition, the sense electrodes are connected by rigid trusses constructing a single sense-frame, increasing the stiffness of the sense electrodes against the spurious deflections caused by the large vibration amplitudes along the drive-mode. Also the flexures of the sense frame are located such that the sense frame is highly robust against rotary oscillations.

Figure 2 shows the layout of the mode-decoupled gyroscope, drawn in Cadence design environment. The gyroscope occupies an area of 3.6x4.0mm2 including the bonding pads, while the die size is about

4.2x4.6mm2. Clearly, the structure is not completely symmetric along the drive and sense modes except the flexures associated with each mode, which have symmetric geometries to minimize temperature-dependent drifts. The use of a single and rigid movable sense-frame suppresses the unwanted coupling motions significantly. Number of the sense fingers is maximized without increasing the footprint too much, by reducing the dead-zones. The movable masses are perforated with circular etch holes with 60µm-diameter, for easy removal of the sacrificial metal layer at the end of the process.

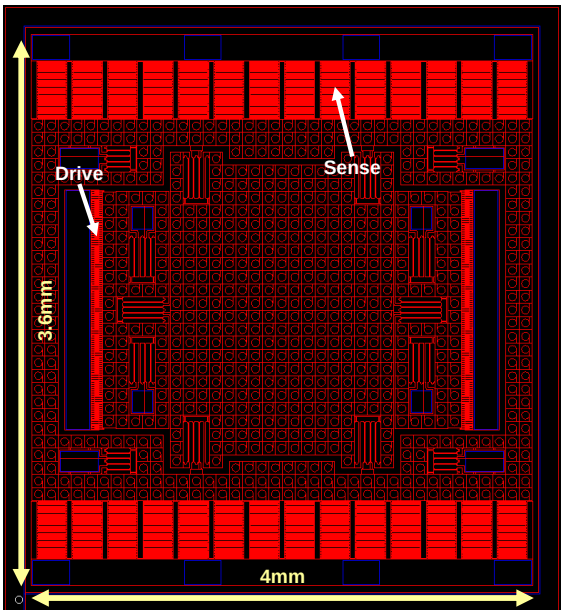

Figure 2: Layout of the mode-decoupled gyroscope, drawn in Cadence design environment. The gyroscope occupies an area of 3.6x4.0mm^2 including the bonding pads, while the die size is about 4.2x4.6mm^2.

Figure 3 shows the exaggerated visualization of the FEM simulation showing the maximum displacement of the sense-mode fingers is less than 500ppm of the drive-mode displacement. In addition, the separation between the resonance frequencies of the operational modes (the drive and the sense modes) and the higher-order modes is improved by increasing the rotational stiffness of the sense electrodes.

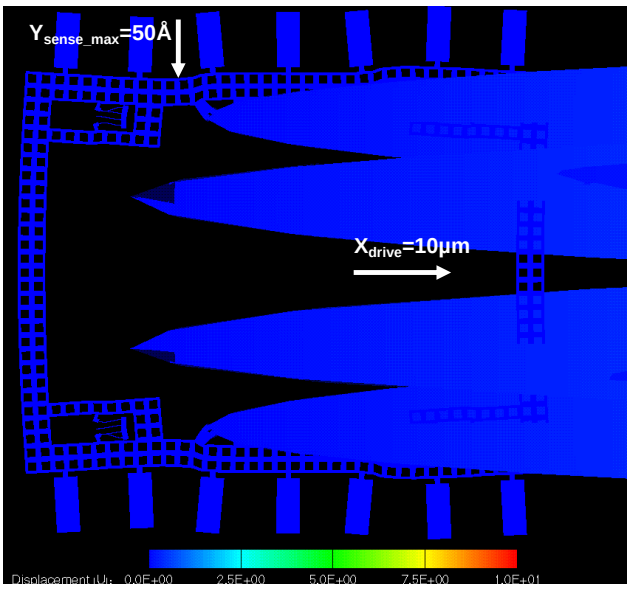

Figure 3: Exaggerated visualization of the FEM simulation showing the maximum displacement of the sense-mode fingers is less than 500ppm of the drive-mode displacement.

Figure 4 shows the first four mode shapes of the designed gyroscope including the drive and the sense modes as well as the nearest two higher order modes, which have the potential for disturbing the operation in the case of any manufacturing flaws. Table 1 provides the resonance frequency associated with each mode. Obviously, the resonance frequencies of the dangerous higher-order modes are highly separated from that of the drive and the sense mode, ensuring a safe operation.

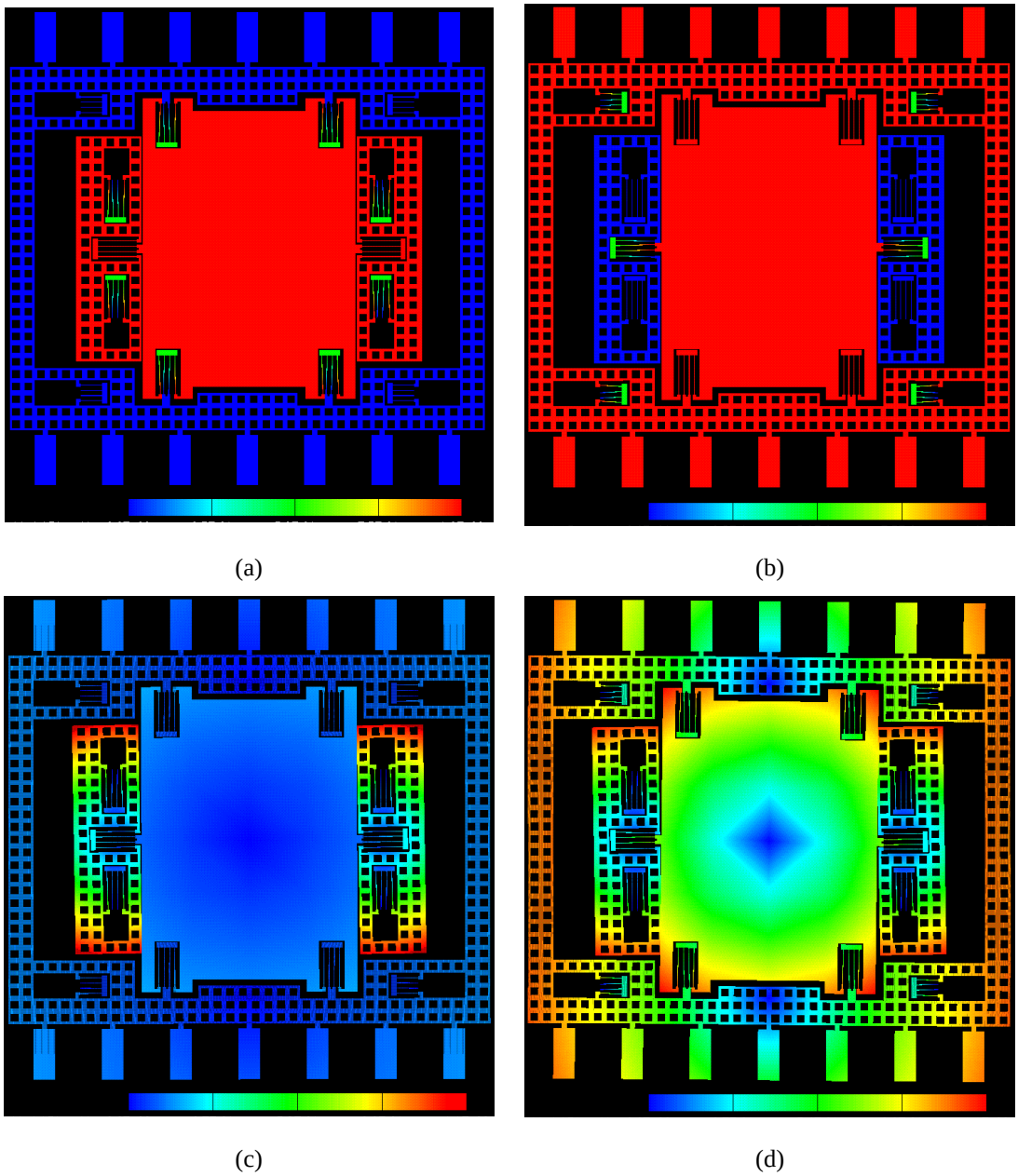

(a) (b)

(c) (d)

Figure 4: The first four mode shapes of the designed gyroscope including the drive and the sense modes as well as the nearest two higher order modes, which have the potential for disturbing the operation in the case of any manufacturing flaws.

3. Fabrication Process

Silicon-on-glass (SOG) micromachining is based on fabricating microstructures defined by thorough-etching of a thin silicon substrate anodically-bonded to a machined glass substrate [4, 15]. Thorough-etching of the silicon substrate is performed by deep ractive ion etching (DRIE), for which aspect ratios higher than 30 are reported [15]. The SOG micromachining process is appropriate for the fabrication of very-thick and high-

aspect-ratio silicon microstructures on low-loss insulating glass substrates, yielding highly-sensitive capacitive inertial sensors with low mechanical-thermal noise and small parasitic capacitances.

Table 1: Simulated resonance frequencies associated with the first four modes.

MODE	GENERALIZED MASS (KG)	RESONANCE FREQUENCY (HZ)
DRIVE	7.49×10^{-7}	5,328
SENSE	1.26×10^{-6}	7,168
ROTARY (DRIVE-ELECTRODES)	9.39×10^{-8}	20,155
ROTARY	6.45×10^{-7}	22,436

The key technology used in SOG micromachining is DRIE, an advanced dry silicon etching technology using inductively coupled plasma patented by Robert Bosch GmbH. The process allows deep and anisotropic silicon etching, by switched etching and passivation cycles. Figure 5 describes the method for anisotropic silicon etching using DRIE (Bosch process). The method relies on the successive passivation coating and silicon etching steps. A thin passivation layer is coated on the whole surface following each etch cycle. The passivation on the surface exposed to the ion bombardment is removed in the next etch cycle; while the passivation on the sidewalls protect lateral etching, resulting in highly anisotropic etch profile with a small sidewall roughness.

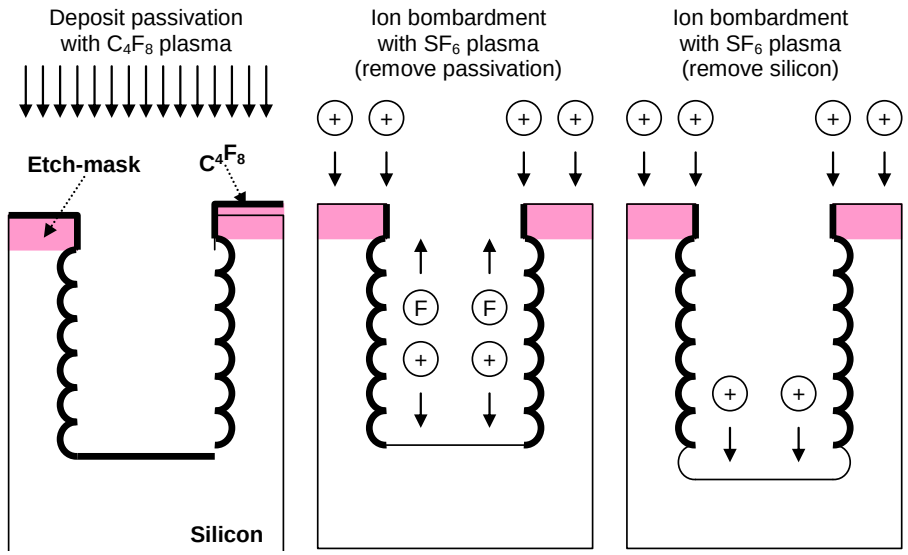

Figure 5: The method for anisotropic silicon etching using DRIE (Bosch process).

There are two important effects about DRIE process, namely microloading and aspect-ratio-dependent etch (ARDE), which needs special care during fabrication otherwise causing permanent damage on the fabricated structures. Microloading refers to the fast etch-rate in an isolated trench compared to the etch-rate for a dense array composed of similar trenches. ARDE effect refers to the fast etch-rate in a wide trench compared to the etch-rate in a narrow trench. Figure 6 illustrates the cross-section of a sample DRIE etch profile, showing the effect of etch-rate variation for different-size trench-openings. The effect of the etch-rate-variation becomes apparent for the through etching of a silicon layer located on top of an insulating substrate. The ions passing through an etched cavity and reaching to the base cause charging of the insulator surface, which can increase the charged potential to several tens of volts [16-18]. The ions are then deflected from the charged insulator surface from the sidewalls, destroying the etch-anisotropy at the bottom of the trench. This effect is called SOI notching, and causes significant destruction of the etched microstructures.

In summary, the features surrounded with large trench openings are subject to damage due to notching, while waiting for the completion of the etch of the features surrounded by narrow trench openings. Figure 7 describes the mechanism of SOI notch and shows the resulting destruction at the bottom of a comb electrode array, a flexure beam, and an etch hole.

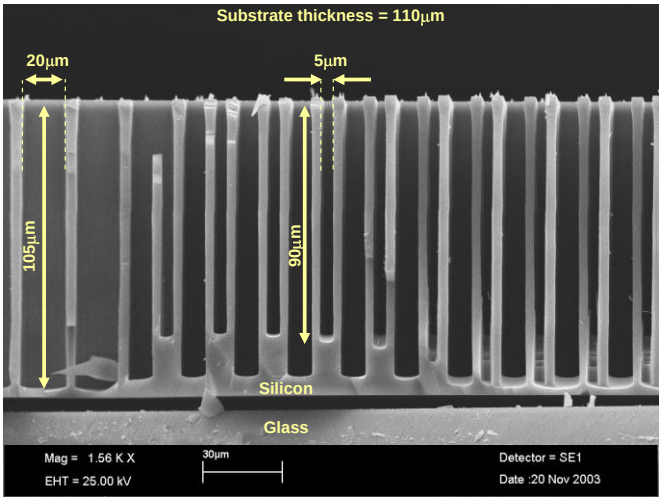

Figure 6: Cross-section of a sample DRIE etch profile, showing the effect of etch-rate variation for different-size trench-openings.

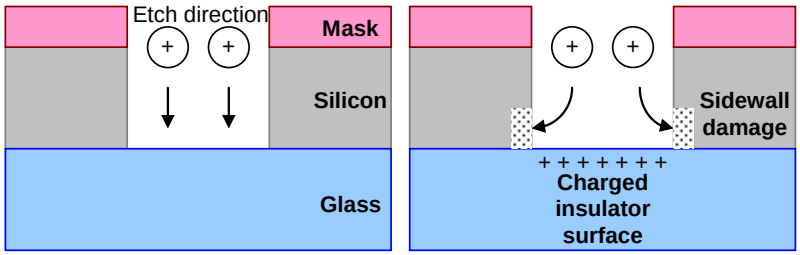

(a)

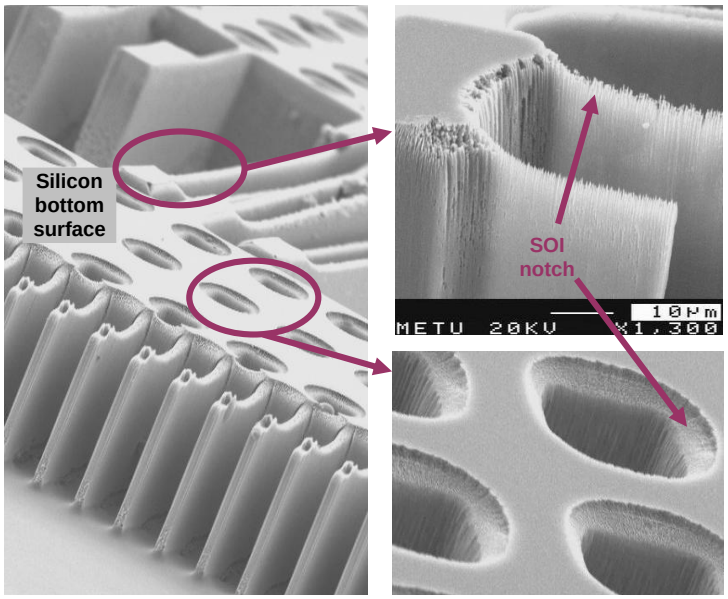

(b)

Figure 7: (a) The mechanism of SOI notch and (b) the resulting destruction at the bottom of a comb electrode array, a flexure beam, and an etch hole.

Insufficient cooling of the silicon substrate during long through-wafer etch period is another factor that can destroy the fabricated structures. The silicon substrate is cooled through the glass substrate, which is kept at a process temperature of about 10°C during DRIE. However, small contact area between the etched silicon substrate and the handling glass substrate reduces efficient heat transfer and results in erosion of the photoresist etch-mask, destroying the sidewalls of silicon features. Figure 8 shows the SEM pictures showing the results of the sidewall destruction for a beam structure fabricated with the improved SOG process.

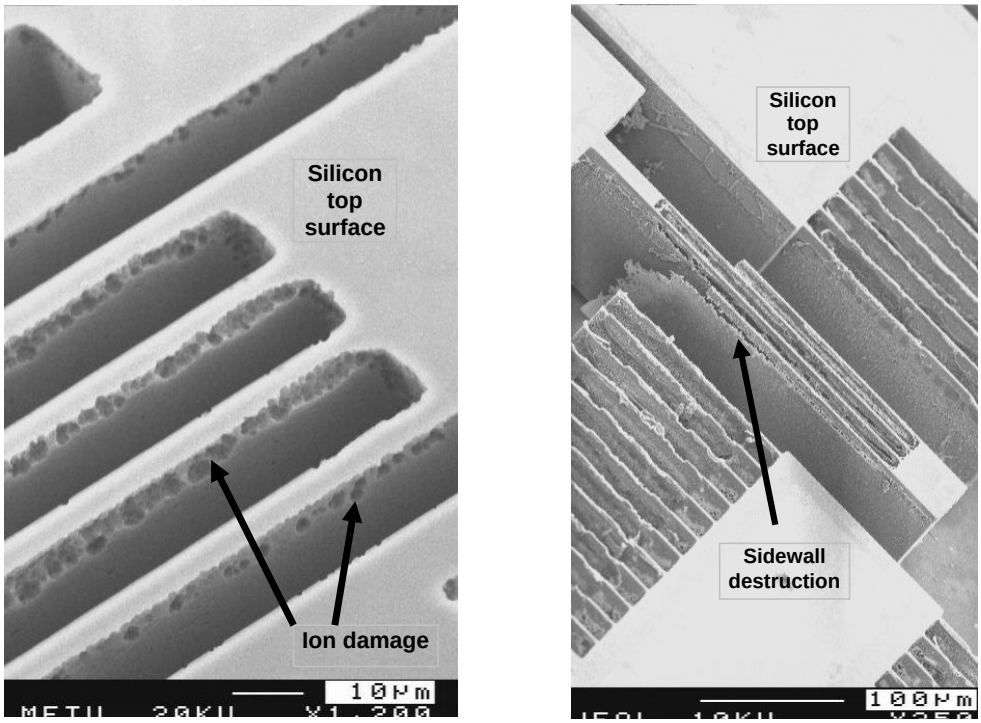

(a) (b)

Figure 8: SEM pictures showing the results of the sidewall destruction for a beam structure fabricated with the improved SOG process: (a) Ion damage at the edges due to reduced mask selectivity. (b) Sidewall destruction.

SOI-notch and mask erosion problems of typical SOG process is eliminated by using an advanced SOG process, for which the metal shield is laid directly at the bottom surface of the silicon substrate instead of the glass surface [19], which acts both as an etch-stop layer against SOI-notch and as a heat sink during DRIE. Figure 9 illustrates the process flow for the SOG process with metal etch-stop layer. The process requires 4 masks and starts with forming anchors on the 500µm-thick, 7740 Pyrex glass substrate. In the meantime, a Cr/Au layer is evaporated on 100µm-thick, highly-conductive blank silicon substrate and is patterned using selective wet etch, defining the metal etch-stop layer. Next, machined silicon and glass substrates are aligned and anodically bonded to each other at 300°C. Following the bonding process, silicon wafer is thoroughly etched by DRIE until the metal etch-stop layer. Then, Cr/Au pad metallization is patterned at the top surface of the silicon substrate. Finally, the sacrificial metal etch-stop layer is removed by protecting the pad metallization; the structures are released.

Figure 10 shows the SEM pictures of microstructures fabricated with the SOG process with metal etch-stop layer, demonstrating (a) no damage due to SOI notch at the bottom surface of the etched silicon around a comb electrode array, flexure, and circular etch holes (b) no significant ion damage at the top surface of the etched silicon around a comb finger array. The capacitive gaps of the fabricated gyroscope are 5.3µm for the drive electrode and 5.6µm for the sense electrode. This yield an aspect ratio close to 20 together with the

100μm silicon structural layer thickness. This high aspect ratio fabrcation process yields a measured sense electrode capacitance of 9.1pF per electrode.

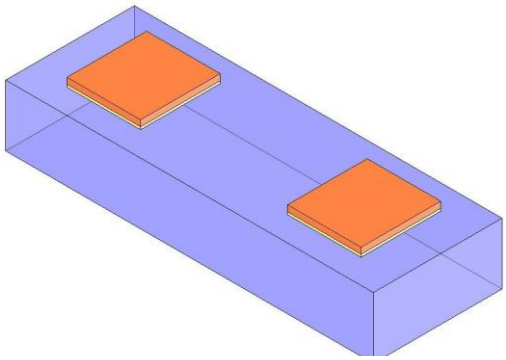

(a) Pattern Cr/Au/PR etch-mask on a blank glass substrate, for glass wet etch

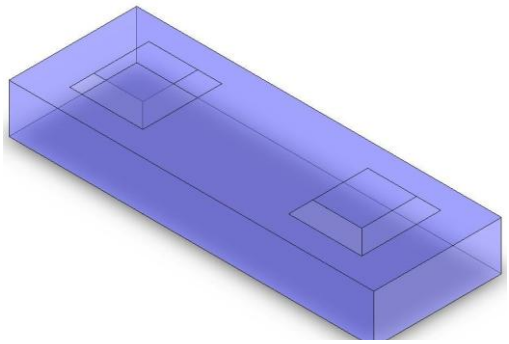

(b) Wet chemical etch of the glass substrate and strip the etch-mask

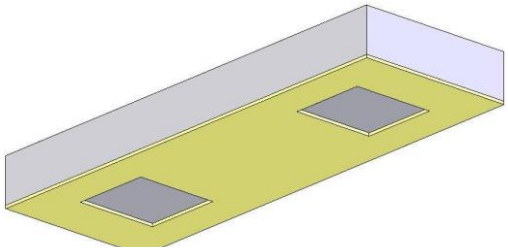

(c) Coat Cr/Au at the bottom surface of the silicon substrate as an etch-stop layer for DRIE.

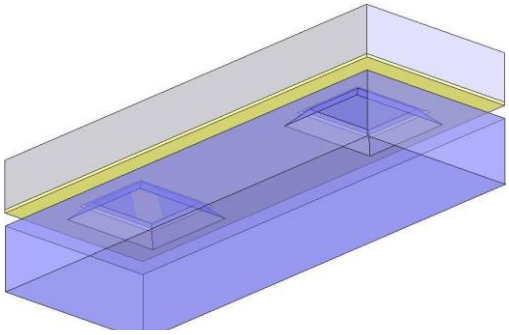

(d) Anodically bond the machined glass and the silicon substrates.

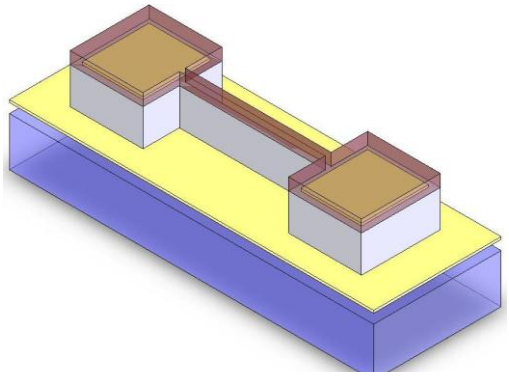

(f) Thorough DRIE etch of the silicon substrate until the metal etch-stop layer.

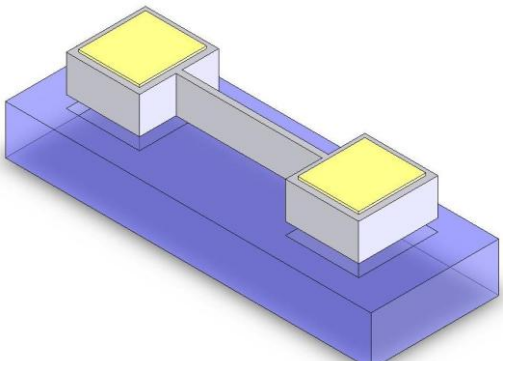

(g) Remove the metal etch-stop layer while protecting pad metallization with DRIE etch-mask, then strip DRIE etch-mask and release the structures

Figure 9: Process flow for the SOG process with metal etch-stop layer.

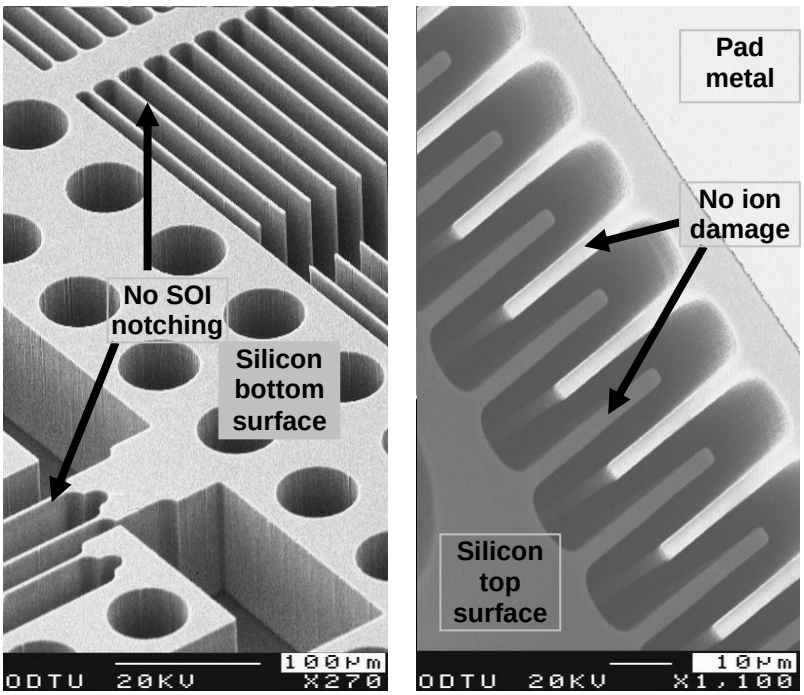

(a) (b)

Figure 10: SEM pictures of microstructures fabricated with the SOG process with metal etch-stop layer, demonstrating (a) no damage due to SOI notch at the bottom surface of the etched silicon around a comb electrode array, flexure, and circular etch holes (b) no significant ion damage at the top surface of the etched silicon around a comb finger array.

4. Characterization of the Fabricated Gyroscope

Figure 11 shows fabricated MEMS gyroscope hybrid-connected to a CMOS capacitive interface circuit, which is fabricated in a standard 0.6µm CMOS foundry process. Resonance frequencies of the fabricated gyroscope are measured with AGILENT 4395A network analyzer at a DC potential of 15^{V} applied to the proof mass. The operating frequency (drive-mode) of the fabricated gyroscope is measured to be close to 2kHz, much smaller than the design value of 5.3kHz. The difference is due to the excessive mask undercut experienced during DRIE of silicon, which makes the fabricated flexures narrower compared to their designed width. This effect is currently under investigation and future mask designs possibly include some means of compensation against this fact. The sense-mode resonance frequency of the gyroscope can be further tuned from 2.45kHz at 5^{V}DC down to 2.02kHz at 16^{V}DC with the help of negative electrostatic springs.

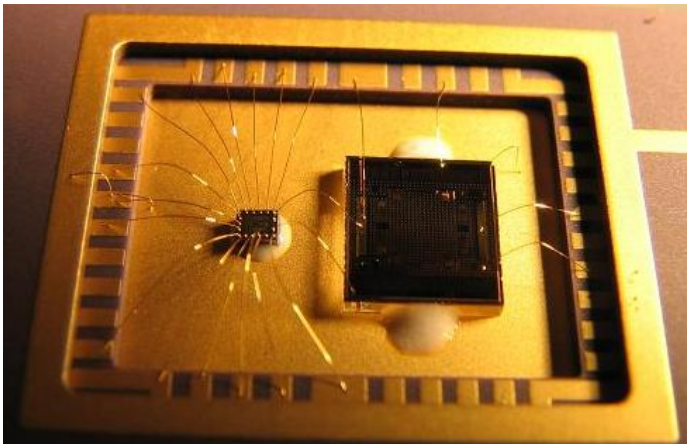

Figure 11: MEMS gyroscope hybrid-connected to a CMOS capacitive interface circuit.

Following preliminary characterization, the gyroscope is driven into self-resonance oscillatins along the drive-mode with closed-loop electronics. Figure 12 shows the required blocks, including the second-order dynamic model of the gyroscope, an AC coupler, a phase shifter, and a final gain stage. The second-order model of the gyroscope includes the dynamics of the drive-mode resonator and the capacitive interface circuit hybrid-connected to the gyroscope. The output of the capacitive interface circuit is filtered through an AC coupler, in order to remove any DC offset coming from the interface circuit. The phase-shifter generates the correct phase for electrostatic actuation to be supplied to the gyroscope input. The final gain stage is necessary to satisfy the overall gain of the system is above unity, so as to cause an amplitude build-up as a result of positive feedback. Closed-loop electronics with automatic amplitude control are currently under development.

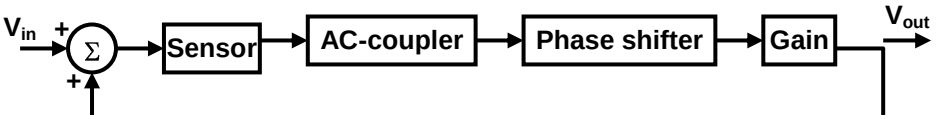

Figure 12: Required blocks for self-resonance excitation of the fabricated gyroscope, including the second-order dynamic model of the gyroscope, an AC coupler, a phase shifter, and a final gain stage.

Following the construction of drive-mode self-resonance electronics, the gyroscope is mounted inside the vacuum chamber of a single-axis rate table. Figure 13-a shows the measured sense-mode raw output of the SOG gyroscope at atmospheric pressure at a proof mass voltage of 19V, and when a sinusoidal angular rate is applied with amplitude 2π deg/sec and frequency 10Hz. The measured rate sensitivity is 15.9μV/(deg/sec), in agreement with the expected value of 15.2μV/(deg/sec) for a proof mass voltage of 19V. Figure 13-b shows the measured sense-mode raw output, when the rate table servo is turned off. The noise floor of the gyroscope is 1.4μVrms/$Hz^{1/2}$, corresponding to 0.09(deg/sec)/$Hz^{1/2}$ rms-noise-equivalent-rate at atmospheric pressure. The measured quadrature signal is less than 60deg/sec due to the advanced-decoupled structure of SOG gyroscope. Still the quadrature signal at atmospheric pressure is dominated by electrical cross-coupling and is further reduced at vacuum operation, verified by the vacuum measurements.

Figure 14-a shows the measured sense-mode output of the gyroscope in response to a 2π deg/sec sinusoidal angular rate input at 10Hz, measured at vacuum. The gyroscope demonstrates a mechanical sensitivity of 900μV/(deg/sec). The measured quadrature signal is only 15deg/sec at vacuum, about 4 times smaller than the quadrature signal at atmospheric pressure, since the amplitude of drive-mode actuation signals and the resulting electrical coupling significantly reduces at vacuum. Figure 14-b shows the measured RMS noise floor of the gyroscope, which is less than 9μV/$Hz^{1/2}$, corresponding to an rms-noise-equivalent rate better than 36deg/hr, when no angular rate is applied to the gyroscope and the servo of the rate table is off.

The decoupled nature of the developed gyroscope structure reduces the amount of quadrature coupling to less than few tens of deg/sec as expected. This is believed to improve the bias stability of the final angular rate sensor significantly, together with automatic amplitude control. Figure 15 shows the Allan variance plot of the mode-decoupled SOG gyroscope driven with an automatic amplitude control loop, which yields an angular random walk of 0.42deg/√hr and bias instability better than 30deg/hr.

Mode-decoupled gyroscope fabricated with silicon-on-glass micromachining process and driven-with amplitude-control drive-mode electronics is believed to demonstrate an overall performance better than 10deg/hr within the end of year 2007.

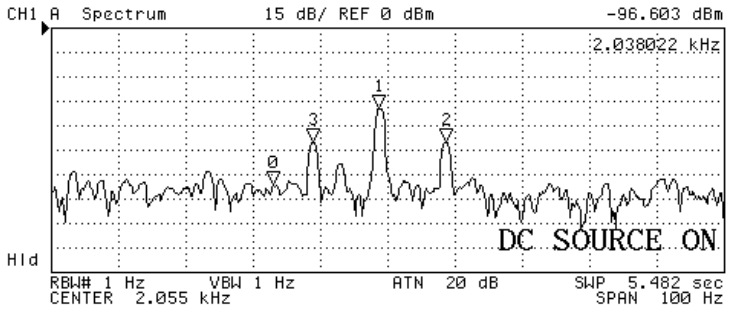

(a)

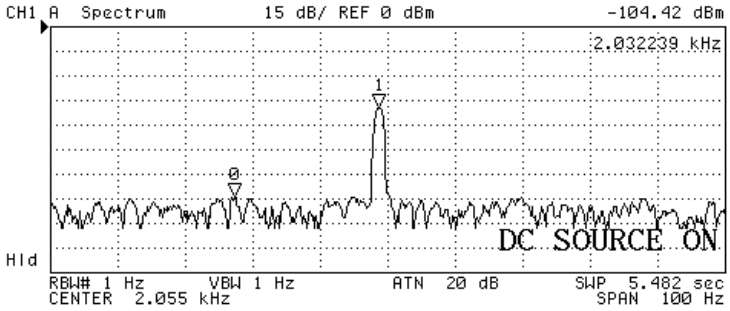

(b)

Figure 13: Measured sense-mode raw output of the SOG gyroscope at atmospheric pressure (a) when a sinusoidal angular rate is applied with amplitude 2π deg/sec and frequency 10Hz (b) when the rate table servo is turned off.

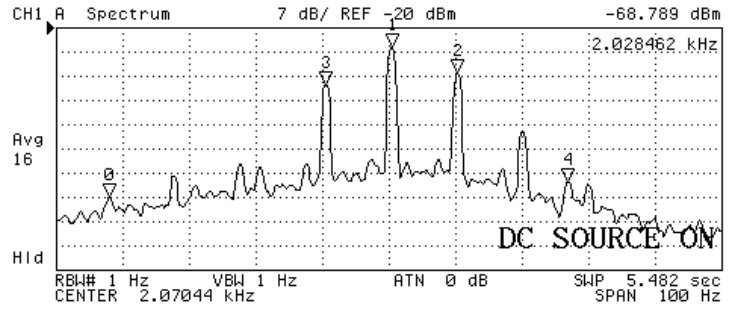

(a)

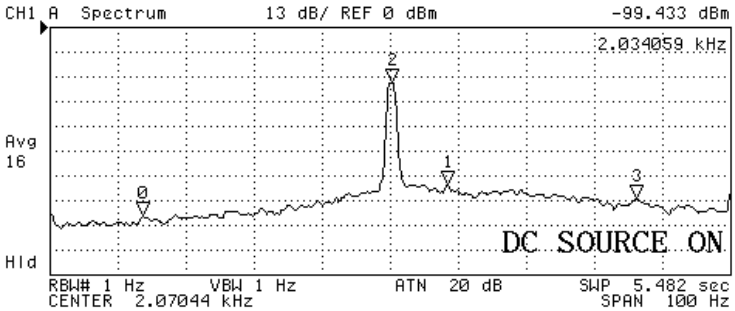

(b)

Figure 14: Measured sense-mode raw output of the SOG gyroscope at vacuum (a) when a sinusoidal angular rate is applied with amplitude 2π deg/sec and frequency 10Hz (b) when the rate table servo is turned off.

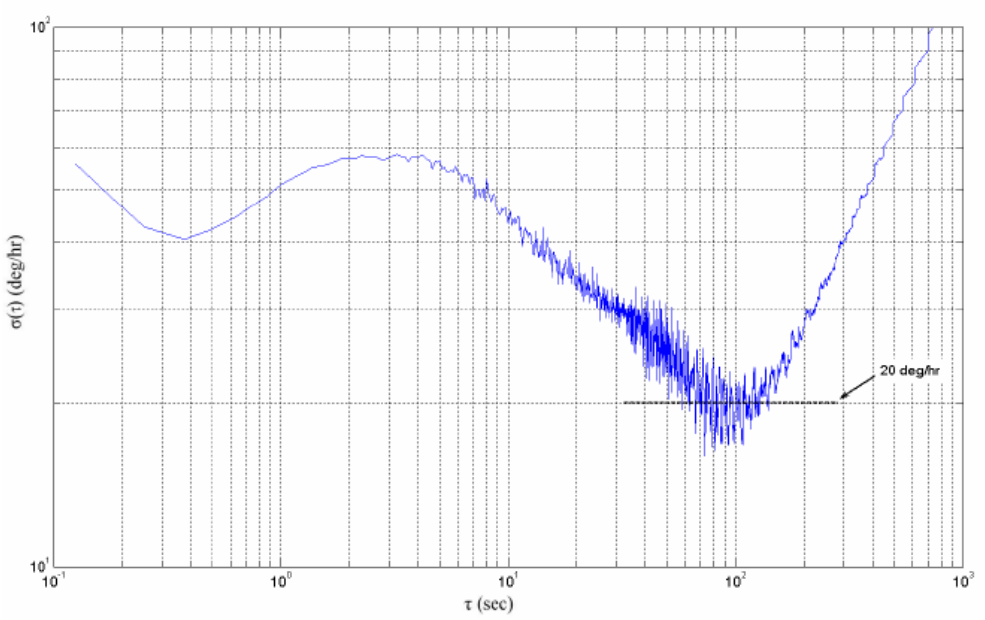

Figure 15: Allan variance plot of the mode-decoupled SOG gyroscope driven with an automatic amplitude control loop, which yields an angular random walk of 0.42deg/√hr and bias instability better than 30deg/hr.

5. Conclusions

This paper presents a 100µm-thick silicon microgyroscope with a special decoupling arrangement between the movable drive and sense electrodes in order to minimize mechanical cross-talk and resulting quadrature coupling between the modes. In addition, the structure is designed for achieving linear drive mode oscillations as high as 10µm and the resonance frequencies of the sense mode can be tuned for matched-mode operation in order to enhance the rate sensitivity. The gyroscope is fabricated in a special silicon-on-glass fabrication process, eliminating parasitic capacitances associated with standard SOI fabrication processes, and it allows the use of very-thick structural layers limited by the silicon substrate thickness and the limitations of dry anisotropic etching. The process includes DRIE thorough etching of a 100µm-thick silicon substrate anodically bonded to a glass substrate, while the heating and SOI footing effects of through-wafer DRIE are eliminated by using a metal etch-stop layer. The gyroscope has capacitive electrodes with an aspect ratio about 20, which provides a huge sense capacitance of about 10pF per differential sense electrodes in a die area less than 20mm^2. The fabricated gyroscope is hybrid connected to a CMOS capacitive interface ASIC fabricated in a commercial 0.6µm CMOS process. A positive-feedback loop force the drive-mode to start self-oscillations whereas the sense-mode is characterized with open-loop signal processing electronics. The cross-coupling between the drive and sense modes of the fabricated gyroscope is measured to be less than 60deg/sec at atmospheric pressure, limited by the electrical crosstalk due to large actuation voltages. Reducing actuation voltages at vacuum also reduces the electrical crosstalk and the gyroscope demonstrates an uncompensated quadrature coupling of only 15deg/sec at 50mTorr vacuum. The measured angular rate sensitivity and the RMS noise-equivalent-rate of the fabricated gyroscope are measured to be 900µV/(deg/sec) and 36(deg/hr)/Hz$^{1/2}$, respectively, at vacuum ambient. The use of automatic amplitude control for the drive-mode self-oscillation electronics improves the overall noise figure and the stability of the gyroscope, yielding an angle random walk of 0.42deg/√hr and bias instability better than 30deg/hr, estimated from the Allan variance analyses.

6. Acknowledgement

This research is funded by the State Planning Organization and The Research and Development Department of Ministry of National Defense. The authors would like to thank Mr. Yuksel Temiz for his helps with the construction of automatic amplitude control electronics and for the generation of Allan Variance plots.

References

[1] K. Funk, H. Emmerich, A. Schilp, M. Offenberg, R. Neul, and F. Larmer, "A Surface Micromachined Silicon Gyroscope Using a Thick Polysilicon Layer," Proc. 12th IEEE Int. Conf. Micro Electro Mechanical Systems Workshop (MEMS'99), Orlando, FL, January 1999, pp. 57-60.

[2] S. Chang, M. Chia, P. Castillo-Borelley, W. Hidgon, Q. Jiang, J. Johnson, L. Obedier, M. Putty, Q. Shi, D. Sparks, and S. Zarabadi, "An Electroformed CMOS Integrated Angular Rate Sensor," Sensors Actuators A, vol. 66, pp. 138-143, April 1998.

[3] M. Weinberg, J. Connely, A. Kourepenis, and D. Sargent, "Microelectromechanical Instrument and Systems Development at the Charles Stark Draper Laboratory," AIAA/IEEE Digital Avionics Systems Conf., October 1997, pp. 8.5.33-8.5.40.

[4] G. He and K. Najafi, "A Single-Crystal Silicon Vibrating Ring Gyroscope," Proc. 15th IEEE Int. Conf., Las Vegas, CA, January 2002, pp. 718-721.

[5] G. T. Schmidt, "INS/GPS Technology Trends," NATO RTO Sensors & Electronics Technology (RTO-SET) Panel: Symp. Emerging Military Capabilities Enabled by Advances in Navigation Sensors (SET'02), Istanbul, Turkey, October 2002.

[6] J. A. Geen, S. J. Sherman, J. F. Chang, and S. R. Lewis, "Single-Chip Surface Micromachined Intergated Gyroscope with 50°/h Allan Deviation," J. Solid State Cct., Vol. 37, No. 12, pp. 1860-1866, December 2002.

[7] W.A.Clark, R.T. Howe, and R. Horowitz, "Surface Micromachined Z-Axis Vibratory Rate Gyroscope," Solid-State Sensor and Actuator Workshop, Hilton Head, California, 2-6 June 1996, pp. 283-289.

[8] M. Palaniapan, R. T. Howe, and J. Yasaitis, "Performance Comparison of Integrated Z-Axis Frame Microgyroscopes," Proc. IEEE Micro Electro Mechanical Systems Workshop (MEMS'03), Kyoto, Japan, January 2003, pp. 482-485.

[9] F. Ayazi and K. Najafi, "A HARPSS Polysilicon Vibrating Ring Gyroscope," J. Microelectromechanical Sys., Vol. 10, No. 2, pp. 169-179, June 2001.

[10] W. Geiger, W. U. Butt, A. Gai□er, J. Frech, M. Braxmaier, T. Link, A. Kohne, P. Nommensen, H. Sandmaier, and W. Lang, "Decoupled Microgyros and the Design Principle DAVED," Sensors Actuators A, vol. 95, pp. 239-249, 2002.

[11] M. S. Kranz and G. K. Fedder,"Micromechanical Vibratory Rate Gyroscopes Fabricated in Conventional CMOS," Symp. Gyro Tech., 1997, pp. 3.0–3.8.

[12] S. E. Alper and T. Akin, "A Symmetrical and Decoupled Nickel Microgyroscope on Insulating Substrate," Sensors and Actuators A, Vol. 115, pp. 336-350, September 2004.

[13] S. E. Alper and T. Akin, "A Single-Crystal Silicon Symmetrical and Decoupled MEMS Gyroscope on an Insulating Substrate," J. Microelectromechanical Systems, Vol. 14, No. 4, pp. 707-717, August 2005.

[14] S. E. Alper, K. Azgin, and T. Akin, "High-Performance SOI-MEMS Gyroscope with Decoupled Oscillation Modes," Proc. 19th IEEE Int. Conf. Micro Electro Mechanical Systems (MEMS 2006), Istanbul, Turkey, 22-26 January 2005, pp. 70-73.

[15] J. Chae, H. Kulah, and K. Najafi, "A Hybrid Silicon-on-Glass (SOG) Lateral Micro-Accelerometer with CMOS Readout Circuitry," in Proc. IEEE Micro Electro Mechanical Systems Workshop (MEMS'02), Las Vegas, CA, January 2002, pp. 623-626.

[16] J. C. Arnold and H. H. Sawin, "Charging of Pattern Features During Plasma Etching," J. Appl. Phys. Vol. 70, No. 10, pp. 5314-5317, November 1991.

[17] G. S. Hwang and K. P. Giapis, "Aspect-Ratio-Dependent Charging in High-Density Plasmas," J. Appl. Phys. Vol. 82, No. 2, pp. 566-571, July 1997.

[18] T. Kinoshita, M. Hane, and J. P. McVittie, "Notching as an Example of Charging in Uniform High Density Plasmas," J. Vac. Sci. Technol. B, Vol. 14, No.1, pp. 560-565, January/February 1996.

[19] C.-H. Kim, J. Park, N. Park, and Y.-K. Kim, "MEMS Fiber-Optic Variable Optical Attenuator Using Collimating Lensed Fiber," IEEE/LEOS Int. Conf. on Optical MEMS, Waikoloa, HI, August 2003, pp. 145-146.